J|A|C|S
ARTICLES
Published on Web 11/18/2006

Chemical Reaction-Inspired Crystal Growth of a Coordination Polymer toward Morphology Design and Control

Shigeyuki Masaoka,[†] Daisuke Tanaka,[†] Hiroyuki Kitahata,[§] Sumiko Araki,[§] Ryotaro Matsuda,[†] Kenichi Yoshikawa,[§] Kenichi Kato,[‡] Masaki Takata,[‡] and Susumu Kitagawa*,[†]

Contribution from the Department of Synthetic Chemistry and Biological Chemistry, Graduate School of Engineering, Kyoto University, Katsura, Nishikyo-ku, Kyoto 615-8510, Japan, Department of Physics, Graduate School of Science, Kyoto University, Kitashirakawa-Oiwakecho, Sakyo-ku, Kyoto 606-8502, Japan, and JASRI/SPring-8, Koto, Hyogo 679-5198, Japan

Received July 22, 2006; E-mail: kitagawa@sbchem.kyoto-u.ac.jp

Abstract: This paper reports a novel crystal growth system of a coordination framework $\{[Cu_3(CN)_3\{hat\text{-}(CN)_3(OEt)_3\}]\}_n$ (**1**) (hat-$(CN)_3(OEt)_3$ = 2,6,10-tricyano-3,7,11-triethoxy-1,4,5,8,9,12-hexaazatriphenylene). The coordination polymer is crystallized through the reaction of 2,3,6,7,10,11-hexacyano-1,4,5,8,9,12-hexaazatriphenylene (hat-$(CN)_6$), ethanol, and copper(I) complex, involving the breaking and forming of covalent bonds. The crystal morphologies obtained in the present system contain dumbbells, cogwheels, and superlattices. Moreover, in the growth perpendicular to the *c*-axis, periodic ramification at regular interval is observed, affording superlattice morphologies. Observation of the growth of dumbbell crystals shows that the growth rates parallel and perpendicular to the crystallographic *c*-axis are quite different: the former shows a drastic change with the reaction duration, while the latter is almost constant. These results are reproduced as a simple reaction−diffusion system, indicating that chemical reactions on crystal surfaces play an important role in determining the macroscopic crystal morphologies.

Introduction

Outside the realm of biology, one of the most beautiful and familiar examples of spontaneous pattern formation in nature can be found in the growth of crystals, regarded as an example of self-organization.[1,2] Nearly everyone is familiar with snow crystals and has been fascinated by their beauty.[3,4] The dendritic morphologies of crystals,[5−9] including snow crystals, are formed by a competition between symmetrical order reflecting the crystal structures and morphological instabilities arising from nonlinear transport processes.[10] In snow crystal formation, the transport process is the diffusion of water molecules toward the crystal.[3,4,11] The patterns of dendritic crystals are generically similar to those found in processes such as viscous fingering and electrochemical deposition.[5−7]

In addition to aesthetic and scientific interests, the morphologies of crystals have attracted much attention in the technological world, because morphologies play an important role in determining properties of crystalline materials.[12−14] Hence, the control of crystal morphologies is currently a key challenge in developing crystalline solids into intelligent materials. The crystal morphologies are formed by a competition between orderly and disorderly growth, and therefore the existence of kinetic process that causes morphological instabilities leads to the formation of characteristic morphological patterns reflecting the symmetry of crystal structure. For example, Figure 1 illustrates some expected morphologies of crystals with two-dimensional hexagonal lattice when growth rate, direction, and their time-dependent change are controlled.

In the present study, we show a crystal growth system involving the crystallization through the breaking and forming of covalent bonds, as a novel approach to control crystal growth rate, direction, and their time-dependent changes. When the crystallization goes through the chemical reaction on the crystal surface, the kinetics of the reaction depends not only on the

[†] Graduate School of Engineering, Kyoto University.
[‡] Graduate School of Science, Kyoto University.
[§] JASRI/SPring-8.

(1) Ball, P. *The Self-made Tapestry: Pattern Formation in Nature*; Oxford University Press: New York, 1999.
(2) (a) Ben-Jacob, E.; Levine, H. *Nature* **2001**, *409*, 985−986. (b) Ben-Jacob, E.; Garik, P. *Nature* **1990**, *343*, 523−530.
(3) Nakaya, U. *Snow Crystals, Natural and Artificial*; Harvard University Press: Cambridge, 1954.
(4) Libbrecht, K. G. *Eng. Sci.* **2001**, *1*, 10−19.
(5) Langer, J. S. *Science* **1989**, *243*, 1150−1156.
(6) Ben-Jacob, E.; Shmueli, H.; Shochet, O.; Tenenbaum, A. *Physica A* **1992**, *187*, 378−424.
(7) Langer, J. S. *Rev. Mod. Phys.* **1980**, *52*, 1−28.
(8) Gránásy, L.; Pusztai, T.; Warren, J. A.; Douglas, J. F.; Börzsönyi, T.; Ferreiro, V. *Nat. Mater.* **2003**, *2*, 92−96.
(9) (a) Ferreiro, V.; Douglas, J. F.; Warren, J.; Karim, A. *Phys. Rev. E* **2002**, *65*, 051606. (b) Ferreiro, V.; Douglas, J. F.; Warren, J.; Karim, A. *Phys. Rev. E* **2002**, *65*, 042802.
(10) (a) Mullins, W. W.; Sekerka, R. F. *J. Appl. Phys.* **1963**, *34*, 323−329. (b) Mullins, W. W.; Sekerka, R. F. *J. Appl. Phys.* **1964**, *35*, 444−451.
(11) Yokoyama, E.; Kuroda, T. *Phys. Rev. A* **1990**, *41*, 2038−2049.
(12) Cahn, R. W. *The Coming of Materials Science*; Pergamon: Oxford, 2001.
(13) (a) He, G.; Eckert, J.; Löser, W.; Schultz, L. *Nat. Mater.* **2003**, *2*, 33−37. (b) Sozzani, P.; Bracco, S.; Comotti, A.; Simonutti, R.; Valsesia, P.; Sakamoto, Y.; Terasaki, O. *Nat. Mater.* **2006**, *5*, 545−551.
(14) (a) Yablonovitch, E. *Phys. Rev. Lett.* **1987**, *58*, 2059−2062. (b) John, S. *Phys. Rev. Lett.* **1987**, *58*, 2486−2489.

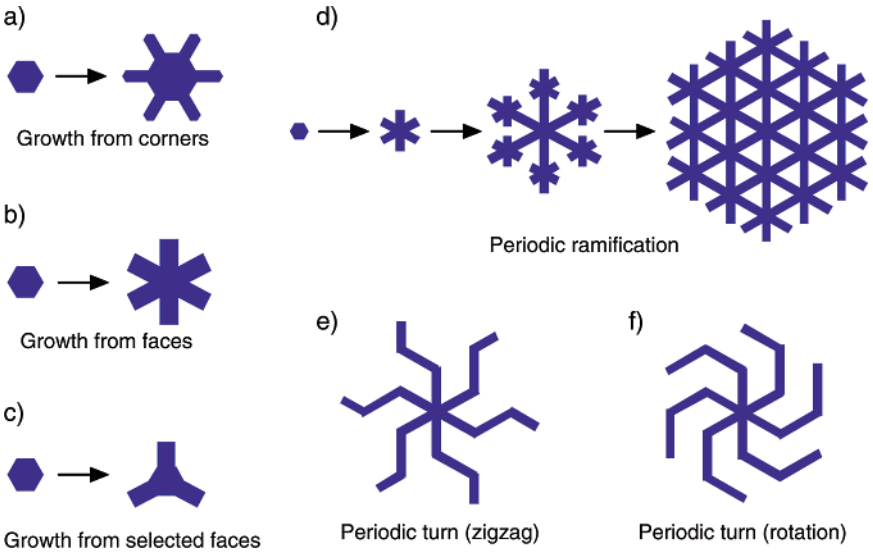

Figure 1. Expected morphologies of crystals with two-dimensional hexagonal lattice when growth rate, direction, and their time-dependent change are controlled. (a−c) Regulation of growth direction. (d−f) Regulation of time-dependent change of growth direction, especially periodic change of growth direction. (a) Crystal growth from corners. When morphological instabilities arise from the nonlinear transport process, this kind of growth occurs (Mullins−Sekerka instabilities). (b) Crystal growth from faces. (c) Crystal growth from selected faces. (d) Periodic ramification into a superlattice morphology. (e,f) Periodic turn into ninja star morphologies.

concentrations of the reactants but also on the crystal surface conditions, such as surface area, roughness, and porosity, resulting in the advent of morphological instabilities. Moreover, the concentrations of the reactants and the crystal surface conditions change during the crystallization, which can lead to the time-dependent changes of the growth rate and direction.

Crystalline materials we are focusing on to control their morphologies are coordination polymers, which are metal−organic hybrid compounds with infinite structures and have been studied in the past decade.[15] In particular, many researches are embedded in the area of utilization of their functions, such as redox property, magnetism, conductivity, spin transitions, catalysis, and porous properties. Very recently, studies on crystal growth control of coordination polymers have been reported, affecting their magnetic[16a−f] and porous[16g] properties. In these systems, crystal size or/and morphology are controlled by the template, such as organic polymer, surfactant, and vesicle.

This paper shows the crystal growth system of a coordination framework $\{[Cu_3(CN)_3\{hat\text{-}(CN)_3(OEt)_3\}]\}_n$ (**1**) (hat-$(CN)_3$-$(OEt)_3$ = 2,6,10-tricyano-3,7,11-triethoxy-1,4,5,8,9,12-hexaazatriphenylene), constructed by the crystallization through the chemical reaction of 2,3,6,7,10,11-hexacyano-1,4,5,8,9,12-hexaazatriphenylene (hat-$(CN)_6$), ethanol, and copper(I) complex. The morphologies of crystals obtained in this system include dumbbell, cogwheel, and superlattice. During the formation of dumbbell crystals, growth rates parallel and perpendicular to the shaft of a dumbbell are quite different: the former shows a drastic change of growth rate, while the latter is almost constant. Cogwheel crystals are formed as a result that the growth rate of the corner is slower than that of the face (Figure 1b), which is obviously an opposite tendency to the growth of common dendritic crystals where the growth rate of the corner is faster than that of the face (Figure 1a).[5−9] Superlattice morphologies are constructed by repeated ramification at regular intervals (Figure 1d) and have never been produced by common dendritic crystals.

Experimental Section

General. ^1H and ^{13}C NMR spectra in $CDCl_3$ solution were recorded on a JEOL A-500 spectrometer operated at 500 MHz, and chemical shifts are reported relative to Me_4Si or residual protons of deuterated solvents. Mass spectra were recorded on a JEOL JMS-SX 102A spectrometer. IR spectra were recorded on a Perkin Elmer 2000 FTIR spectrometer using Nujol mull. X-ray powder diffraction measurement (XRPD) data were collected on a Rigaku RINT 2000 (Ultima) diffractometer by using Cu K_α radiation. XRPD data of skeletal thin plates of **1** were measured by synchrotron powder diffraction with a Debye−Scherre camera. The collected thin plates of **1** were bound between poly(vinyl acetate) films, and X-ray was exposed parallel and perpendicular to the plates. The synchrotron radiation experiments were performed on the BL02B2 beam line at the SPring-8 with the approval of the Japan Synchrotron Radiation Research Institute (JASRI). Single-crystal X-ray diffraction data were measured on a Rigaku/MSC Mercury CCD diffractometer with graphite-monochromated Mo K_α radiation. AFM images were measured via Olympus NVB 100. Photographs of crystals were taken via an Olympus BX51 microscope with a DP70 digital camera. Sequence photographs of crystals were taken via a SONY Digital Handycam.

Materials. Copper(II) acetate monohydrate was purchased from Nakarai Tesque, Inc., and hydroquinone was from Wako Pure Chemical Industries, Ltd. The building block hat-$(CN)_6$ was prepared according to the literature procedure.[18] Tetrahydrofuran (THF), chloroform ($CHCl_3$), methanol (MeOH), ethanol (EtOH), 1-propanol, 2-propanol,

(15) (a) Moulton, B.; Zaworotko, M. J. *Chem. Rev.* **2001**, *101*, 1629. (b) Yaghi, O. M.; O'Keeffe, M.; Ockwig, N. W.; Chae, H. K.; Eddaoudi, M.; Kim, J. *Nature* **2003**, *423*, 705−714. (c) Janiak, C. *Dalton Trans.* **2003**, 2781. (d) Evans, O. R.; Lin, W. *Acc. Chem. Res.* **2002**, *35*, 511−522. (e) Kim, K. *Chem. Soc. Rev.* **2002**, *31*, 96−107. (f) Papaefstathiou, G. S.; MacGillivray, L. R. *Coord. Chem. Rev.* **2003**, *246*, 169−184. (g) Rosseinsky, M. J. *Microporous Mesoporous Mater.* **2004**, *73*, 15−30. (h) James, S. L. *Chem. Soc. Rev.* **2003**, *32*, 276−288. (i) Kitagawa, S.; Kitaura, R.; Noro, S. *Angew. Chem., Int. Ed.* **2004**, *43*, 2334.
(16) (a) Uemura, T.; Kitagawa, S. *Chem. Lett.* **2005**, *34*, 132. (b) Uemura, T.; Kitagawa, S. *J. Am. Chem. Soc.* **2003**, *125*, 7814. (c) Uemura, T.; Ohba, M.; Kitagawa, S. *Inorg. Chem.* **2004**, *43*, 7339. (d) Yamada, M.; Arai, M.; Kurihara, M.; Sakamoto, M.; Miyake, M. *J. Am. Chem. Soc.* **2004**, *126*, 9482. (e) Vaucher, S.; Fielden, J.; Li, M.; Dujardin, E.; Mann, S. *Nano Lett.* **2002**, *2*, 225. (f) Dominguez-Vera, J. M.; Colacio, E. *Inorg. Chem.* **2003**, *42*, 6983. (g) Uemura, T.; Hoshino, Y.; Kitagawa, S.; Yoshida, K.; Isoda, S. *Chem. Mater.* **2006**, *18*, 992−995.
(17) Tanaka, D.; Masaoka, S.; Horike, S.; Furukawa, S.; Mizuno, M.; Endo, K.; Kitagawa, S. *Angew. Chem., Int. Ed.* **2006**, *45*, 4628−4631.

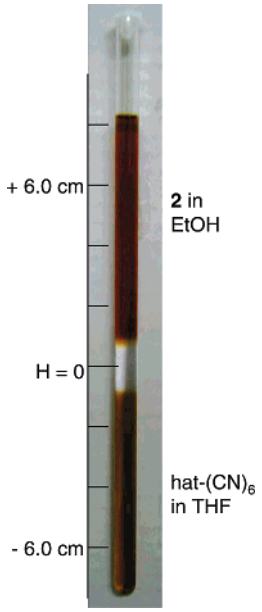

Figure 2. Method of crystallization. The center of the middle layer (THF/ethanol layer) was marked as the zero point ($H = 0$), and the signs, + and −, indicate the upper and lower sides, respectively.

benzyl alcohol, 1-dodecanol, and *l*-menthol were obtained from Wako Pure Chemical Industries, Ltd., and used without any purification.

Synthesis of hat-$(CN)_3(OEt)_3$. The THF solution of hat-$(CN)_6$ was added to the EtOH solution of $[Cu^I_2(\mu_2\text{-}\eta^2,\eta^2\text{-benzoquinone})(OAc)_2]$ (**2**),[19] and then the mixture was refluxed for 2 h, where the resulting dark brown suspension contains a coordination framework $\{[Cu_3(CN)_3\text{-}\{\text{hat-}(CN)_3(OEt)_3\}]\}_n$ (**1**), identified by XPRD and IR. After extraction with $CHCl_3$, recrystallization from THF/EtOH afforded the C_3 symmetrical isomer of hat-$(CN)_3(OEt)_3$ as pale yellow needles (yield 13%). ^{1}H NMR ($CDCl_3$): $\delta = 1.66$ (t, $J = 7.5$ Hz, 9H, methyl), 4.96 (q, $J = 7.5$ Hz, 6H, methylene). ^{13}C NMR ($CDCl_3$): $\delta = 14.21$ ($-CH_3$), 66.08 ($-CH_2-$), 113.60 ($-$CN), 122.61 (external Ar, root of cyano group), 133.22 (internal Ar), 142.58 (internal Ar), 160.46 (external Ar, root of ethoxy group). MS(FAB): $m/z = 442$ (M + 1). IR (Nujol): 2235 cm^{-1} (CN stretch). Crystals suitable for single-crystal X-ray crystallography were obtained by recrystallization from DMF/EtOH.

Crystal Structure of hat-$(CN)_3(OEt)_3$ (Figure 3). All data were measured on a Rigaku/MSC Mercury CCD diffractometer with graphite-monochromated Mo K_α radiation. The structure was solved by direct methods (SIR 97). All calculations were performed with the TEXSAN crystallographic software package.

X-ray Structure Determination of hat-$(CN)_3(OEt)_3$. All non-hydrogen atoms were refined anisotropically. Refinement was carried out with full-matrix least-squares on the absolute value of *F*. Crystal data for hat-$(CN)_3(OEt)_3$, $C_7H_{10}N_3O$: $M_r = 152.18$, crystal size 0.40 × 0.03 × 0.01 mm, monoclinic, space group *C*2/*c* (No. 15), $a = 23.42(2)$ Å, $b = 14.925(9)$ Å, $c = 15.20(1)$ Å, $\beta = 128.983(9)°$, $V = 4128(4)$ Å^3, $Z = 24$, $\rho_{calcd} = 1.469$ g/cm^3, λ(Mo K_α) = 0.71070 Å, $F(000) = 1944.00$, μ(Mo K_α) = 1.03 cm^{-1}, $T = -20$ °C, $2\theta_{max} = 55.0°$, of the 194 69 reflections that were collected, 4610 were unique ($R_{int} = 0.040$); equivalent reflections were merged. For 2246 reflections with $I > 4.00\sigma(I)$, 298 parameters; $R(R_w) = 0.079(0.074)$. GOF = 1.61. The residual electron density (min/max) is −0.29/0.38 e$^-$/Å.^{3}

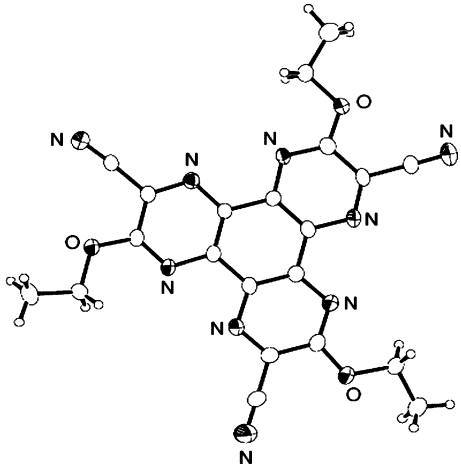

Figure 3. Crystal structure of hat-$(CN)_3(OEt)_3$ (showing 30% anisotropic thermal ellipsoids).

Synthesis of hat-$(CN)_3(OR)_3$ Derivatives. The following hat-$(CN)_3(OR)_3$ derivatives were synthesized in ways similar to that of hat-$(CN)_3(OEt)_3$. All compounds were identified by ^{1}H,^{13}C NMR and/or first atom bombardment (FAB) mass spectrometry. **hat-$(CN)_3(OCH_3)_3$.** ^{1}H NMR ($CDCl_3$): $\delta = 4.47$ (s, 9H, methyl). ^{13}C NMR ($CDCl_3$): $\delta = 56.47$ ($-CH_3$), 113.47 ($-$CN), 122.67 (external Ar, root of cyano group), 133.41 (internal Ar), 142.50 (internal Ar), 160.77 (external Ar, root of methoxy group). MS(FAB): $m/z = 400$ (M + 1). **hat-$(CN)_3(OCH_2CH_2CH_3)_3$.** ^{1}H NMR ($CDCl_3$): $\delta = 1.18$ (t, $J = 7.5$ Hz, 9H, methyl), 2.05 (m, 6H, methylene), 4.84 (t, $J = 6.5$ Hz, 6H, methylene). ^{13}C NMR ($CDCl_3$): $\delta = 10.41$ ($-CH_3$), 21.98 ($-CH_2-$), 71.45 ($-OCH_2-$), 113.56 ($-$CN), 122.59 (external Ar, root of cyano group), 133.21 (internal Ar), 142.58 (internal Ar), 160.60 (external Ar, root of ethoxy group). MS(FAB): $m/z = 484$ (M + 1). **hat-$(CN)_3(OCH(CH_3)_2)_3$.** ^{1}H NMR ($CDCl_3$): $\delta = 1.61$ (d, $J = 6.0$ Hz, 18H, methyl), 5.95 (septet, $J = 6.0$ Hz, 3H, methine). ^{13}C NMR ($CDCl_3$): $\delta = 21.69$ ($-CH_3$), 74.09 ($-OCH-$), 113.78 ($-$CN), 122.73 (external Ar, root of cyano group), 133.00 (internal Ar), 142.66 (internal Ar), 160.09 (external Ar, root of ethoxy group). MS(FAB): $m/z = 484$ (M + 1). **hat-$(CN)_3(OCH_2C_6H_5)_3$.** ^{1}H NMR ($CDCl_3$): $\delta = 5.91$ (s, 6H, methylene), 7.36−7.75 (m, 15H, phenyl). ^{13}C NMR ($CDCl_3$): $\delta = 71.23$ ($-OCH_2-$), 113.53 ($-$CN), 122.76 (external Ar, root of cyano group), 128.71 (phenyl), 129.03 (phenyl), 129.44 (phenyl), 133.51 (internal Ar), 134.14 (phenyl), 142.34 (internal Ar), 160.14 (external Ar, root of ethoxy group). MS(FAB): $m/z = 628$ (M + 1). **hat-$(CN)_3(O(CH_2)_{11}CH_3)_3$.** ^{1}H NMR ($CDCl_3$): $\delta = 0.79-1.95$ (m, 23H, alkyl), 4.80 (t, $J = 6.5$ Hz 6H, methylene). MS(FAB): $m/z = 862$ (M + 1). **hat-$(CN)_3(OR')_3$ (R′OH = *l*-menthol).** MS(FAB): $m/z = 772$ (M + 1).

$[Cu_3(CN)_3(\text{hat-}(CN)_3(OEt)_3)]_n$ (1). The identification of **1** was carried out by single-crystal X-ray structure determination, elemental analysis, and infrared absorption spectrum. For the structural details, see ref 17.

Crystallization. The crystallization was performed by a slow intermixing of a solution of hat-$(CN)_6$ in THF and **2** in ethanol by diffusion (Figure 2). A solution of hat-$(CN)_6$ (10 mM, 2 mL) in THF was placed in a long Pyrex tube with a 6 mm internal diameter. An ethanol solution of **2** (10 mM, 2 mL), prepared by the in situ reaction of copper(II) acetate with hydroquinone in ethanol,[19] was carefully layered on top of the hat solution in THF, followed by layering 0.5 mL of the mixed solvent THF/ethanol (1:1 v/v) of intermediate density. To demonstrate that the crystal was growing, we defined an *H* value that shows the ordinate along the glass tube. The center of the middle layer (THF/ethanol layer) was marked as the zero point ($H = 0$), and the signs, + and −, indicate the upper and lower sides, respectively (Figure 2).

(18) (a) Rademacher, J. T.; Kanakarajan, K.; Czarnik, A. W. *Synthesis* **1994**, 378. (b) Kanakarajan, K.; Czarnik, A. W. *J. Heterocycl. Chem.* **1998**, *25*, 1869. (c) Beeson, J. C.; Fitzgerald, L. J.; Gallucci, J. C.; Gerkin, R. E.; Rademacher, J. T.; Czarnik, A. W. *J. Am. Chem. Soc.* **1994**, *116*, 4621.
(19) (a) Masaoka, S.; Akiyama, G.; Horike, S.; Kitagawa, S.; Ida, T.; Endo, K. *J. Am. Chem. Soc.* **2003**, *125*, 1152−1153. (b) Masaoka, S.; Tanaka, D.; Nakahishi, Y.; Kitagawa, S. *Angew. Chem., Int. Ed.* **2004**, *43*, 2530−2534.

Scheme 1

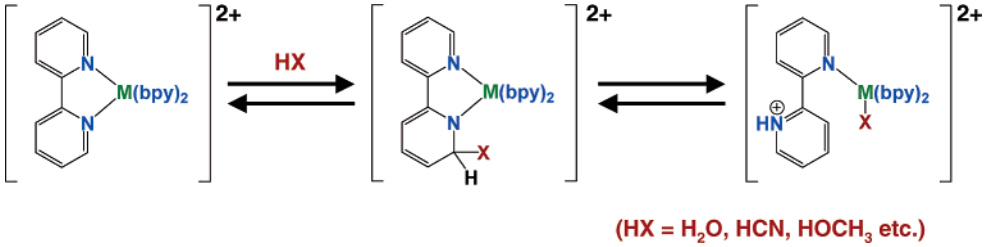

Scheme 2

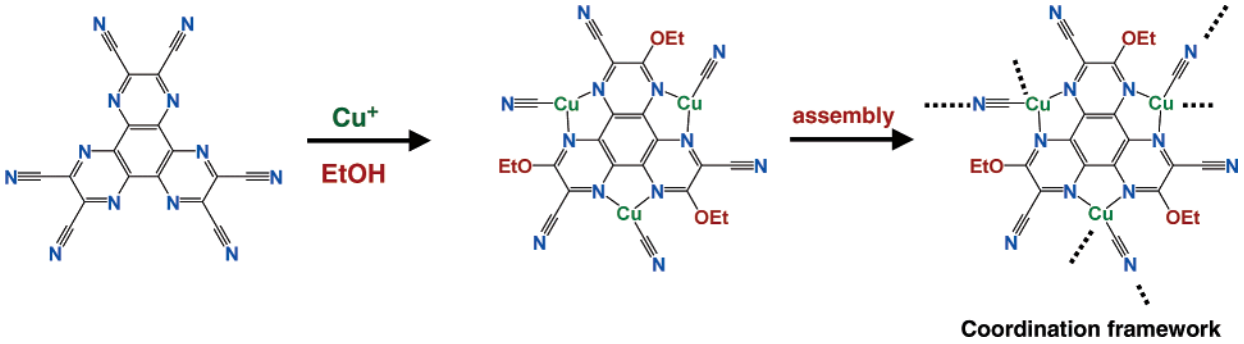

Results

Reaction. As the chemical reaction simultaneous with crystal growth, the nucleophilic displacement reaction characteristic of *N*-heterocyclic chelate ligands such as 2,2′-bipyridine (bpy) and 1,10-phenanthroline (phen) was used. Coordination of *N*-heterocyclic chelate ligands to a metal ion has an effect similar to quaternization and consequently activates the α-carbon atoms of the ligands for nucleophilic attack.[20,21] The process of quaternizating is illustrated in Scheme 1 for a typical $[M(bpy)_3]^{2+}$ complex. In our study, this reaction was applied to hexaazatriphenylene (hat) derivatives, which are C_3 symmetrical *N*-heterocyclic chelate ligands and have been studied as attractive supramolecular building blocks to date.[22,23]

Scheme 2 illustrates the construction of the coordination framework through the breaking and forming of covalent bonds. The reaction of a hexacyano derivative of hat, hat-$(CN)_6$,[23] a metal ion, and a nucleophile can afford a coordination framework, because the ligand hat-$(CN)_6$ functions not only as a C_3 symmetrical chelate ligand, but also as a supplier of a linear bridging ligand (CN^-), which can connect two metal ions. Indeed, the reactions of hat-$(CN)_6$, with various alcohols (ROH; for example: methanol, ethanol, 1-propanol, 2-propanol, benzyl alcohol, 1-dodecanol, and *l*-menthol) in the presence of the copper(I) complex $[Cu_2^I(benzoquinone)(OAc)_2]$ (**2**),[19] afford corresponding coordination frameworks containing respective tricyano trialkoxy derivatives of hat, hat-$(CN)_3(OR)_3$, through the substitution of alkoxy groups for cyano groups.[24] Extraction of the ligands with $CHCl_3$ gives respective C_3 symmetrical isomers of hat-$(CN)_3(OR)_3$, identified by ^1H,^{13}C NMR, first atom bombardment (FAB) mass spectrometry, and/or single-crystal X-ray structure analysis (Scheme 3). Figure 3 shows the crystal structure of a triethoxy derivative, hat-$(CN)_3(OEt)_3$.

The crystallization was performed by a slow intermixing of a solution of hat-$(CN)_6$ in THF and **2** in ethanol by diffusion. One week after the diffusion reaction was started, hexagonal columns with pinched-in waists (Figure 4a,b) of $[Cu_3(CN)_3\{hat\text{-}(CN)_3(OEt)_3\}]_n$ (**1**) were obtained in the zone $H = 0.5-2.0$ cm (for the *H* value, see Figure 2). The X-ray diffraction of these dumbbell-like hexagonal columns shows the hexagonal space group ($P6_3/mmc$, No. 194) with the crystallographic *c*-axis along the shaft of the crystals (Scheme 4). In the crystallographic structure of **1** (Figure S1 in the Supporting Information), Cu(I) cations are connected by linear (CN^-) and C_3 symmetrical (hat-$(CN)_3(OEt)_3$) building blocks, forming the three-dimensional coordination network. When the Cu(I) center and the midpoint of hat-$(CN)_3(OEt)_3$ are regarded as three-connecting nodes, the structure of **1** is described as a net with (8,3)-*c* type topology.[25] To the best of our knowledge, the coordination framework **1** is the first example of a three-dimensional coordination network constructed through the breaking and forming of covalent bonds, except for examples synthesized by solvothermal reactions.[26−28]

(20) (a) Gillard, R. D. *Coord. Chem. Rev.* **1975**, *16*, 67−94. (b) Serpone, N.; Ponterini, G.; Jamieson, M. A. *Coord. Chem. Rev.* **1983**, *50*, 209−302.
(21) (a) Zhang, X.-M.; Tong, M.-L.; Chen, X.-M. *Angew. Chem., Int. Ed.* **2002**, *41*, 1029−1031. (b) Zhang, X.-M.; Tong, M.-L.; Gong, M.-L.; Lee, H.-K.; Luo, L.; Li, K.-F.; Tong, Y.-X.; Chen, X.-M. *Chem.-Eur. J.* **2002**, *8*, 3187−3194.
(22) For metal complexes with hat derivatives, see: (a) Kitagawa, S.; Masaoka, S. *Coord. Chem. Rev.* **2003**, *246*, 73. (b) Abrahams, B. F.; Jackson, P. A.; Robson, R. *Angew. Chem., Int. Ed.* **1998**, *37*, 2656. (c) Latterini, L.; Pourtois, G.; Moucheron, C.; Lazzaroni, R.; Brédas, J.-L.; Kirsch-De Mesmaeker, A.; De Schryver, F. C. *Chem.-Eur. J.* **2000**, *6*, 1331. (d) Baxter, P. N. W.; Lehn, J.-M.; Knersel, B. O.; Baum, G.; Feske, D. *Chem.-Eur. J.* **1999**, *5*, 113. (e) Galán-Mascarós, J. R.; Dunbar, K. R. *Chem. Commun.* **2001**, 217. (f) Masaoka, S.; Furukawa, S.; Chang, H.-C.; Mizutani, T.; Kitagawa, S. *Angew. Chem., Int. Ed.* **2001**, *40*, 3817. (g) Grove, H.; Sletten, J.; Julve, M.; Lloret, F. *J. Chem. Soc., Dalton Trans.* **2001**, 1029.
(23) For metal complexes with hat-$(CN)_6$, see: (a) Okubo, T.; Kitagawa, S.; Kondo, M.; Matsuzaka, H.; Ishii, T. *Angew. Chem., Int. Ed.* **1999**, *38*, 931. (b) Furukawa, S.; Okubo, T.; Masaoka, S.; Tanaka, D.; Chang, H.-C.; Kitagawa, S. *Angew. Chem., Int. Ed.* **2005**, *44*, 2700−2704. (c) Okubo, T.; Kitagawa, S.; Masaoka, S.; Furukawa, S.; Kondo, M.; Noh, T.; Isoshima, T.; Wada, T.; Sasabe, H. *Nonlinear Opt.* **2000**, *24*, 129. (d) Szalay, P. S.; Galán-Mascarós, J. R.; Clérac, R.; Dunbar, K. R. *Synth. Met.* **2001**, *122*, 535.
(24) X-ray powder diffraction analysis of the dark brown crystalline solids revealed that these solids have isomorphous structures of three-dimensional coordination framework **1**.
(25) Wells, A. F. *Three-Dimensional Nets and Polyhedra*; Wiley: New York, 1977.
(26) Zheng, N.; Bu, X.; Feng, P. *J. Am. Chem. Soc.* **2002**, *124*, 9688−968.
(27) Tong, M.-L.; Li, L.-J.; Mochizuki, K.; Chang, H.-C.; Chen, X.-M.; Li, Y.; Kitagawa, S. *Chem. Commun.* **2003**, 428−429.
(28) Zhang, X.-M. *Coord. Chem. Rev.* **2005**, *249*, 1201−1219.

Scheme 3

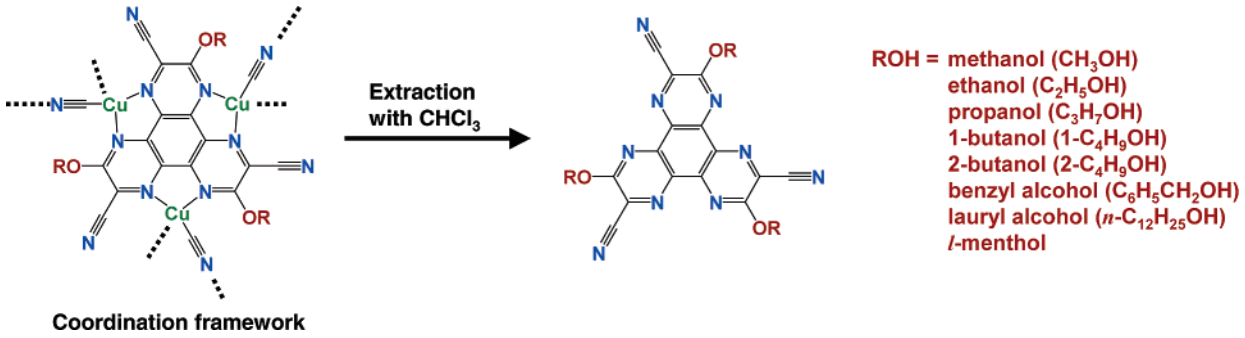

Scheme 4

The projection along the *c*-axis shows a hexagonal honeycomb network whose nodes are occupied by C_3 symmetrical building blocks, hat-$(CN)_3(OEt)_3$. Needless to say, this honeycomb network associates with the hexagonal column morphology of the crystals of **1**.

Morphological Pattern Formation. One week after the diffusion reaction was started, dumbbell-like crystals with various lengths, widths, and depth of hollows were observed in the zone $H = 0.5-2.0$ cm. In the zone $H = 1.0-2.0$ cm, dumbbells with long shafts were obtained, whose length of shaft ranged from 200 to 1000 μm (Figure 4a). On the other hand, short dumbbells with 50−100 μm shafts were observed around the point $H = 0.5$ cm. Figure 4b shows the short dumbbells grown at the point $H = 0.5$ cm.

Figure 5a shows sequence photographs of the growth of one selected crystal of **1**, grown at the point $H = 1.2$ cm. About 30 h after the diffusion reaction was started, a needle crystal of **1** formed. The needle grew longer with the reaction duration. After ca. 100 h, growth along the shaft came to a stop, even though the reactants were supersaturated enough to crystallize. From that point, growth thickening of the needle became dominant. The growth rate at both sides of the shaft was faster than that at the center of the shaft, affording dumbbell-like crystals. Figure 5b shows plots of the dimensions of the crystal displayed in Figure 5a against the reaction time. While the growth rate in the *ab* plane was almost constant, the rate along the *c*-axis showed a marked decrease to zero in ca. 100 h. As shown in Figures S3 and S4 in the Supporting Information, this process is common to all dumbbell crystals.

As the reaction time increased, the two bases of the dumbbell-like crystals of **1** became a cogwheel-like shape with C_6 symmetry. Figure 6 shows the cogwheel-shaped morphology grown at the point $H = 0.5$ cm. It should be emphasized that the growth rate of the corner is slower than that of the face, resulting in unique cogwheel morphologies. This is obviously an opposite tendency to the growth of common dendritic crystals where the growth rate of the corner is faster than that of the face.[5−9] Figure 7 shows the X-ray diffraction pattern of a cogwheel crystal of **1**. The pattern clearly elucidates that the cogwheel crystal is a single crystal, and the six cogs are extending along [100] direction.

Crystallization under a diffusion field of the molecular building blocks can afford a variety of morphologies at the same time according to the *H* value, on which the transport process of the molecular precursors depends. In the zone $H = 2.0-7.0$ cm, the crystals of **1** did not grow significantly along the *c*-axis, affording skeletal thin plates instead of dumbbells. The most remarkable features about the crystal morphologies of **1** were observed in this zone after 4 weeks or more (Figure 8 and Figure S2 in the Supporting Information). Six cogs of the cogwheel-shaped crystals of **1** grew longer, and then ramified along the crystallographic hexagonal lattice at regular intervals, forming micrometer-sized superlattice patterns. The periods of the

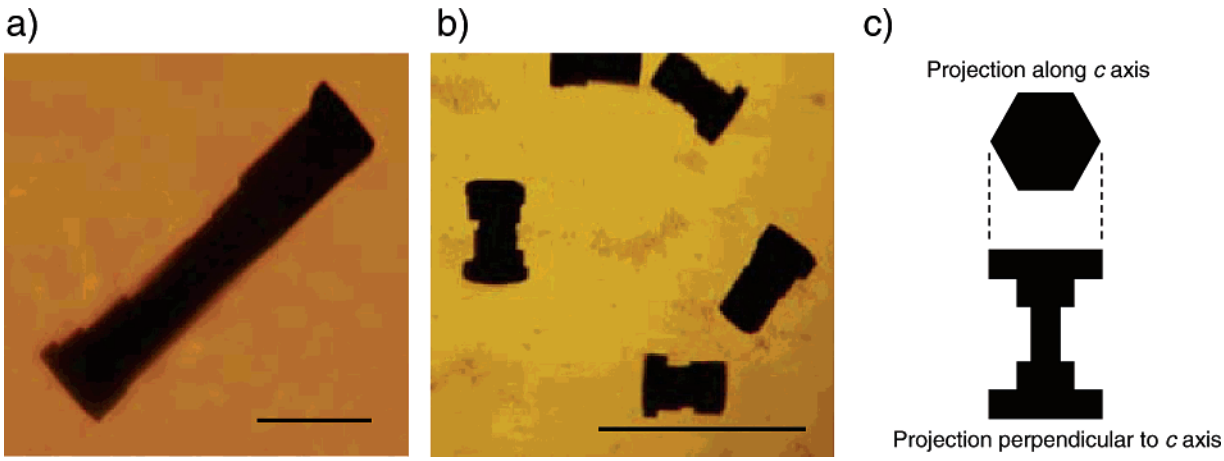

Figure 4. Dumbbell crystals of **1**. (a) A crystal grown at the point $H = 2.0$ cm after 1 week. (b) At $H = 0.5$ cm after 1 week. (c) Schematic representation of the morphology of a dumbbell crystal. (a,b) Scale bars are 100 μm.

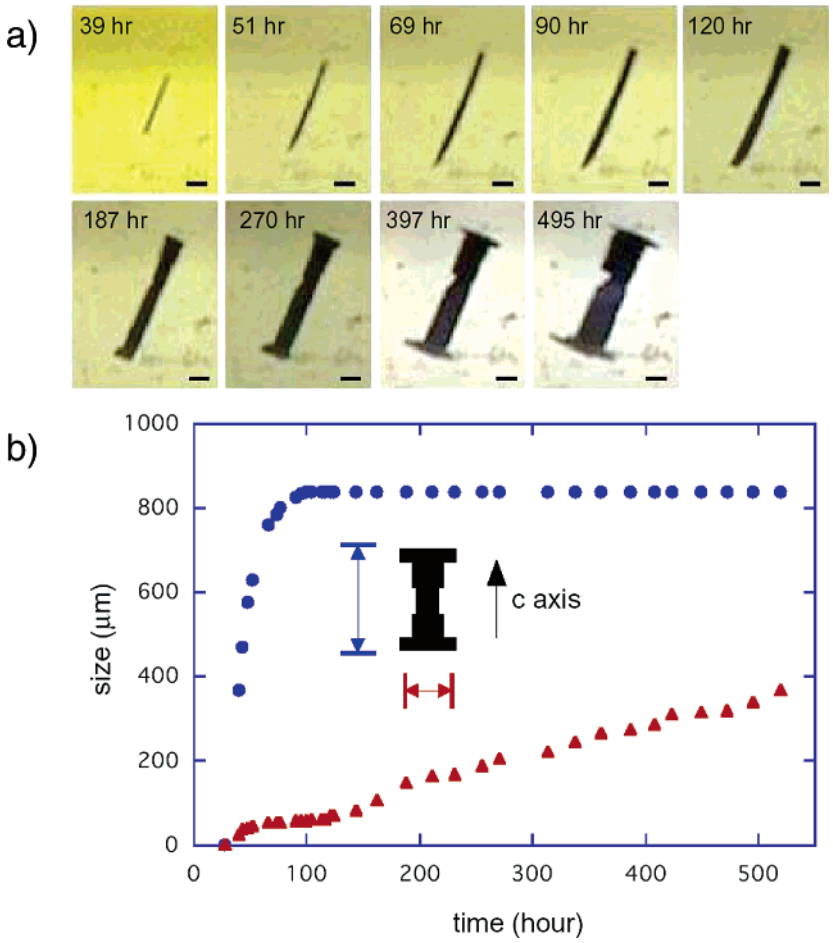

Figure 5. (a) Sequence photographs of a crystal of **1** grown at $H = 1.2$ cm. Scale bars are 100 μm. (b) Plots of the dimensions of the crystal displayed in (a) against the reaction time. Blue circles show the length of the shaft of the dumbbell. Red triangles show the maximum width of the dumbbell.

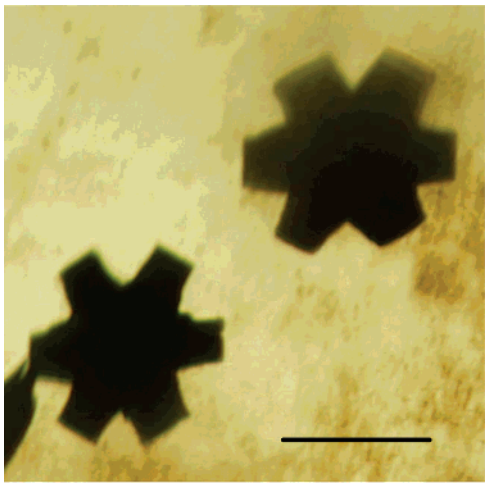

Figure 6. Cogwheel crystals of **1** grown at the point $H = 0.5$ cm after 3 weeks. Scale bar is 100 μm.

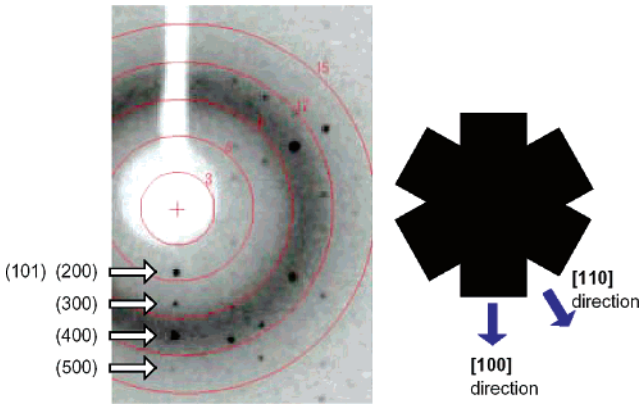

Figure 7. Single-crystal X-ray diffraction data of a cogwheel crystal of **1**. The data were measured on a Rigaku/MSC Mercury CCD diffractometer with graphite-monochromated Mo K_α radiation. The X-ray diffraction pattern clearly shows that the six cogs are extending along [100] direction. Red numbers on the circles represent 2θ values.

superlattice patterns range from ca. 50 to 200 μm, corresponding to ca. $(2.7-11) \times 10^4$ crystallographic unit cells, respectively. Moreover, on the rims of these skeletal hexagonal plates, a stripe pattern perpendicular to the growing direction ([100] direction) often appeared. Because these superlattice and stripe patterns were observed under isothermal conditions (Figure 8c), the periodic growth was not caused by a periodic change of temperature.

Figure 9 shows the X-ray powder diffraction patterns of these skeletal hexagonal plates of **1**, where the X-rays were exposed parallel and perpendicular to the plates. The diffraction patterns confirm that there is no structural change during the growth of crystals and clearly show the effect of preferred orientation, indicating that these skeletal plates are single crystals of **1**.

In addition to the macroscopic observation of crystal morphologies, microscopic patterns on the crystal surface of **1** have been investigated by using atomic force microscopy (AFM).

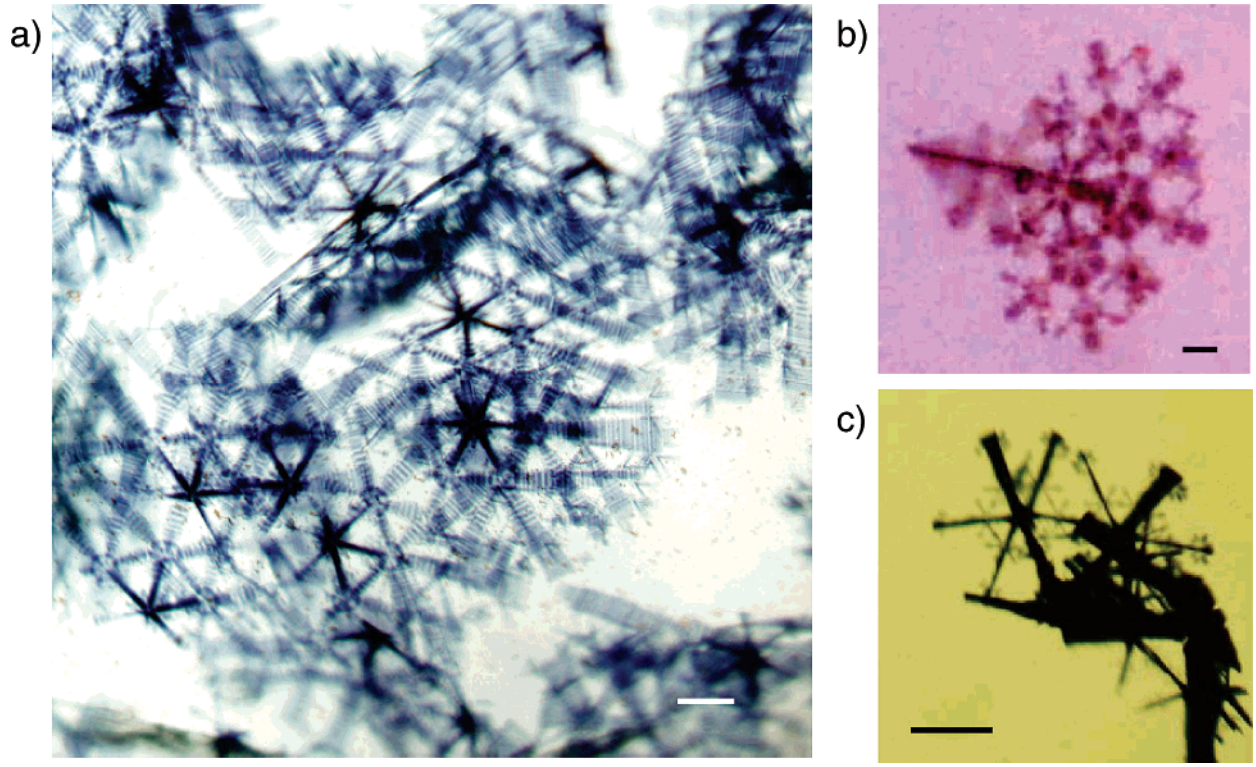

Figure 8. Superlattice crystals of **1**. (a) Grown at the point $H = 6.0$ cm after 2 months. (b) At $H = 6.0$ cm after 3 months. (c) At $H = 4.0$ cm after 2 months. The growth temperature was fixed at 0 °C. (a−c) Scale bars are 100 μm.

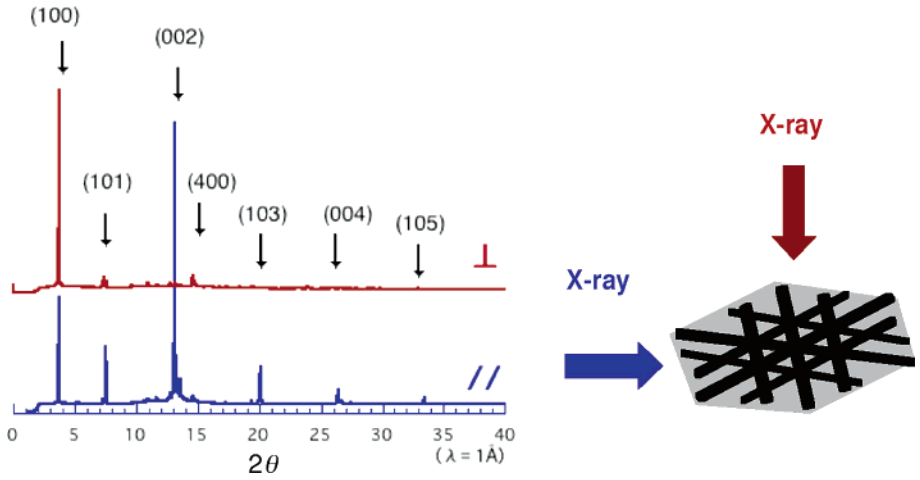

Figure 9. Powder X-ray diffraction data of collected skeletal thin plates of **1**. The data were measured by synchrotron powder diffraction with a Debye−Scherre camera. The collected thin plates of **1** were oriented by binding between poly(vinyl acetate) films, and X-rays were exposed parallel and perpendicular to the plates. X-ray powder diffraction patterns of these skeletal hexagonal plates confirm that there is no structural change during the growth of crystals and clearly show the effect of preferred orientation, indicating that these superlattice crystals are single crystals of **1**. The synchrotron radiation experiments were performed at the SPring-8 with the approval of the Japan Synchrotron Radiation Research Institute (JASRI).

The measurements were performed on (001) faces of thin plate crystals of **1** (Figure 10). The AFM images clearly show that the surfaces of crystals have the microscopic patterns that are closely related to the macroscopic crystal morphologies. As shown in Figure 10a, the arms of the cogwheel crystals have striped patterns along the growing direction, or [100] direction. The striped patterns lead to the centers of hexagonal cogwheels. At the centers of the cogwheels the two neighboring striped patterns lie at an angle of 60° (Figure 10b), affording approximate C_6 symmetrical patterns. On the other hand, a ramification does not occur with C_6 symmetry, like the centers of the cogwheels, but with mirror symmetry along the trunk (Figure 10c). In one junction, there are two branching centers, from which twigs sprout up along the hexagonal lattice in clockwise or anticlockwise rotation. The twigs that lie at angles of 60° and 120° from the trunk grow into bigger branches. The twig at an angle of 180° from the trunk grows and acts as a part of the trunk. Twigs growing at an angle of 240° or greater clash with the trunk, thus stopping their growth. Because these branchings occur at two centers, the trunk has four new branches from one junction.

Figure 11 shows the history of the crystal growth of **1**. First, a crystal grows along the *c*-axis into a needle. The growth extending the needle comes to a stop, and then the needle grows

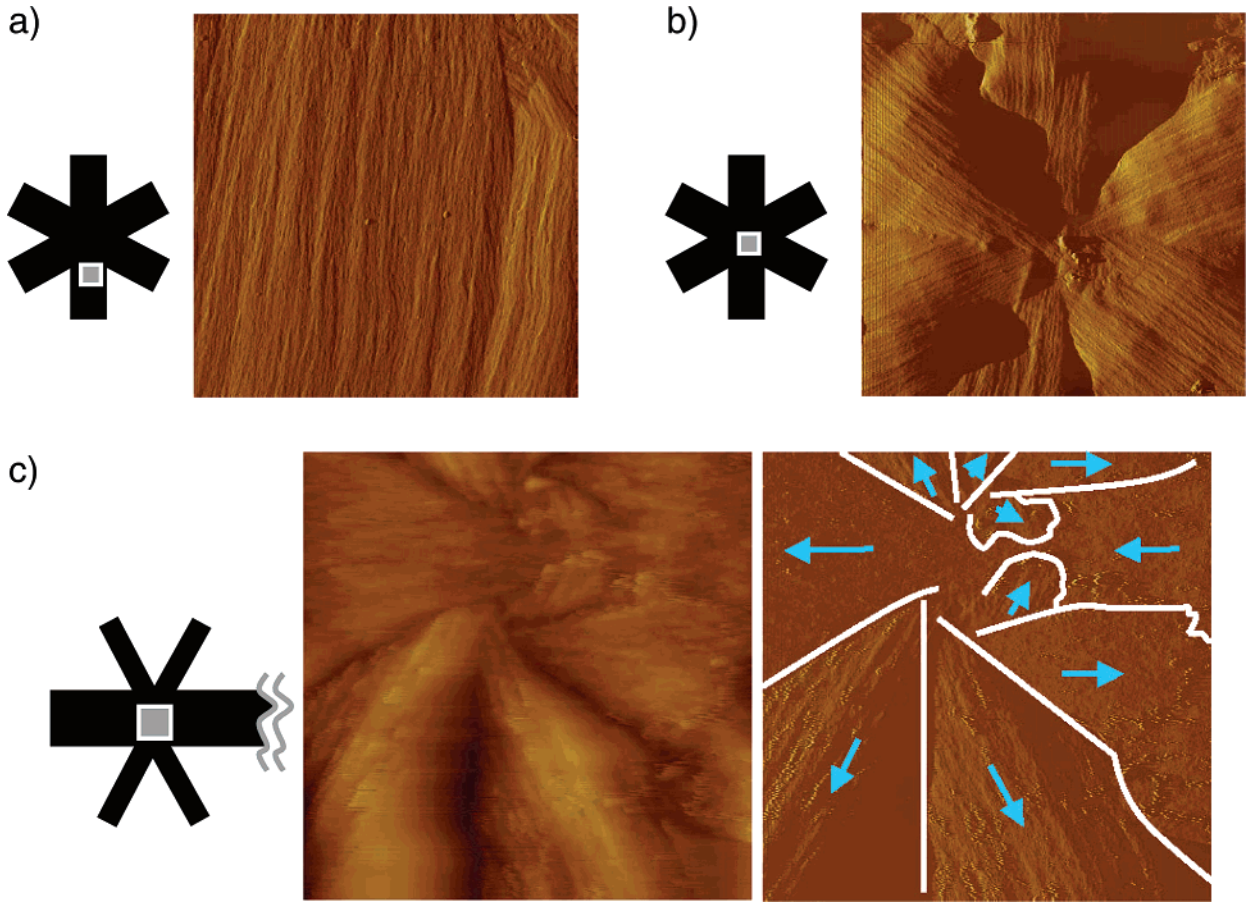

Figure 10. AFM images taken on (001) faces of thin plate crystals of **1**. (a) On a arm of a cogwheel crystal. (b) On the center of a cogwheel crystal. (c) On a branching point. (a−c) The sides of the square images correspond to 10 μm. The images were measured via Olympus NVB100.

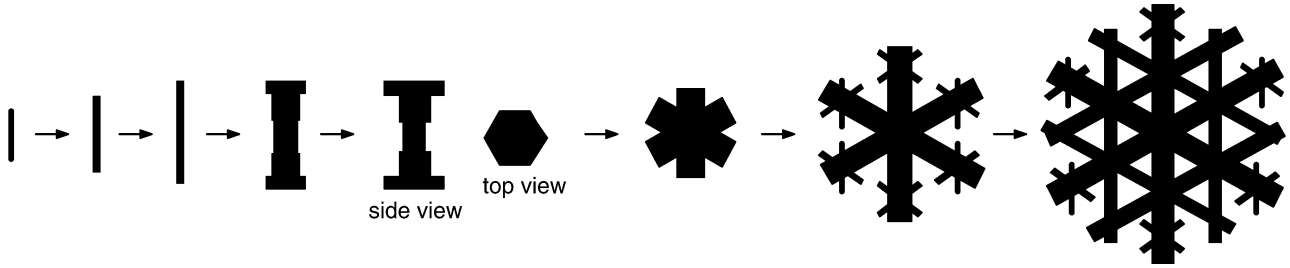

Figure 11. Schematic representation of the history of the crystal growth of **1**.

into a hexagonal dumbbell. Next, the two bases of the hexagonal dumbbell grow to hexagonal cogwheels. The six arms then grow and ramify at regular intervals, forming the superlattice. The ramification occurs at two branching centers, from which twigs sprout up along the hexagonal lattice in clockwise or anticlockwise rotation. In the zone $H = 2.0-7.0$ cm, there is no process to grow along the *c*-axis, affording the skeletal thin plates. Interestingly, during the growth of crystals there is no change of the crystal structure, and these crystals with various morphologies are single crystals.

Discussion

Before the consideration of the crystal growth mechanism, it may be helpful to begin with a brief review of the growth mechanism of snow crystals as an example of dendritic crystals. The big factor affecting snow crystal shape is the diffusion of water molecules through the air. It is easier for the water molecules to diffuse the growing crystal, because the corners of the crystal stick out a bit further into the air than the center faces, resulting in that the corners grow a bit faster than the rest of the crystal surface. As the result, diffusion tends to hinder the crystal growth, and this produces what turns out to be a fairly common effect, known as Mullins−Sekerka instability.[10] The patterns of dendritic crystals are generically similar to those found in processes such as viscous fingering and electrochemical deposition.[5−7]

In the present study, we have observed characteristic morphologies, dumbbell, cogwheel, and superlattice. The cogwheel morphology is formed by that the growth rate of the corner is slower than that of the face, which is obviously an opposite tendency to the growth of common dendritic crystals,[5−9] thus

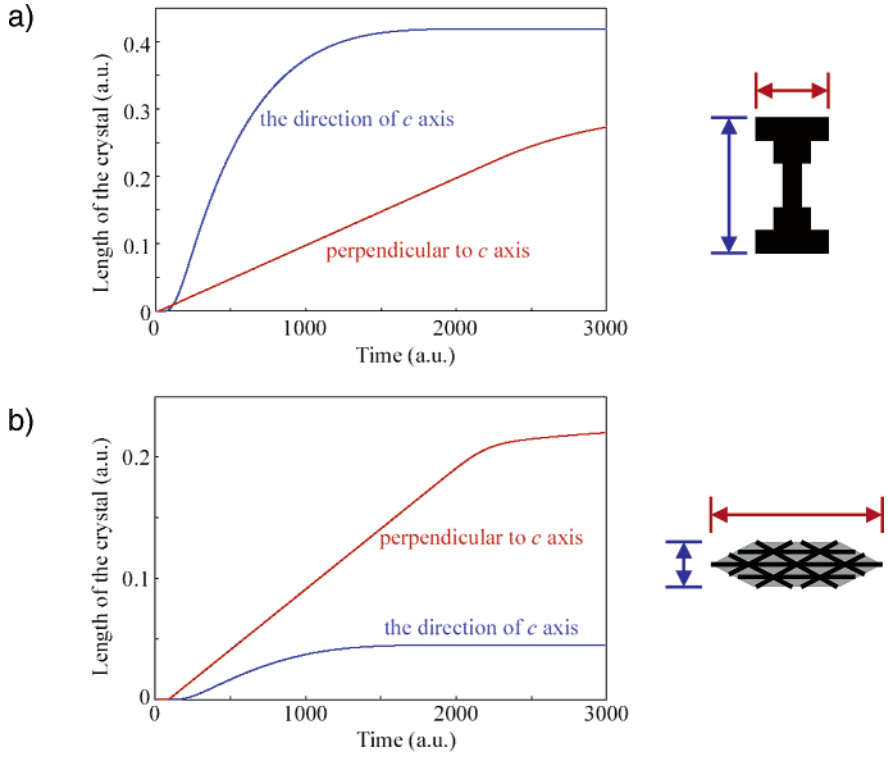

Figure 12. The results of numerical calculation. We used eqs 1a−d and 2a,b. The parameters used here are $k_1 = 1.0$, $k_2 = 10^{-4}$, and $c_0 = 10^{-4}$. The time developments of the crystal lengths parallel and perpendicular to *c*-axis are shown at (a) $H = 0$, (b) $H = L/4$, where L is the total tube length. The result obtained with $H = 0$ (a) corresponds to the experimental profiles shown in Figure 6b.

indicating that the morphological instabilities are caused by the kinetics on the surface rather than by nonlinear transport processes.[10]

To discuss the mechanism of the morphological pattern formation, we especially paid notice to the time-dependent change of growth rates in the formation of dumbbell crystals (Figure 5) on the assumption that *the chemical reaction occurs on the crystal surface and influences the crystal growth rate*. As shown in Figure 5b, the growth rate along the *c*-axis decreases and approaches to zero, as time goes on. On the other hand, the growth rate perpendicular to the *c*-axis is almost constant. Therefore, it is apparent that rate-determining steps of the crystal growth parallel and perpendicular to *c*-axis are different.

The crystal growth along the *c*-axis shows a drastic change of growth rate with the reaction duration and, therefore, may be due to the reaction that proceeds proportionally to the concentrations of reactants. Accompanied by the diffusion of the reactants from both sides of the tube, the concentrations of reactants rapidly increase during the initial stage. Some time later, the reaction rate slows down, because of the attainment of quasi-steady state in the concentrations. This process is thus regarded as a diffusion-limited process.

On the other hand, the growth rate perpendicular to the *c*-axis is almost constant with the reaction duration (Figure 5b) and, therefore, may be determined by the reaction at the crystal surface. In other words, the diffusion that provides the chemicals to the crystal surface is much faster than the consumption by the chemical reaction, and therefore the chemical reaction becomes independent of the concentration. Hence, this can be regarded as a reaction-limited process.

It may be, thus, concluded that the dumbbell-like shaped crystal growth seems to be caused by the two different reaction and diffusion processes.

We considered a simple model given as a set of equations as a reaction−diffusion system.[29] For simplicity, the crystallization process is written as a reaction between two reactants, A and B. In the initial state, these two chemicals locally exist on both sides of the reaction field. As time goes by, these chemicals diffuse and begin to react each other. As for the crystallization along the *c*-axis, we assume that the crystallization process can be written as an auto-catalyst process, because the crystal surface exhibits the role of front on the crystallization. For simplification, the crystallization process along the *c*-axis is written as the square of the product of two chemicals [A][B]. As for in the direction perpendicular to the *c*-axis, we assumed the maximum rate of crystallization, because of the slow process of the crystallization. In other words, over the critical concentration around the crystal, the growth rate is almost independent of the concentration. We take the exponential saturation to the maximum value.

From these considerations, we adopt the following equations:

$$\frac{\partial[\mathrm{A}]}{\partial t} = D\nabla^2[\mathrm{A}] - f_c([\mathrm{A}],[\mathrm{B}]) - f_p([\mathrm{A}],[\mathrm{B}]) \quad (1a)$$

$$\frac{\partial[\mathrm{B}]}{\partial t} = D\nabla^2[\mathrm{B}] - f_c([\mathrm{A}],[\mathrm{B}]) - f_p([\mathrm{A}],[\mathrm{B}]) \quad (1b)$$

$$\frac{\partial l_c}{\partial t} = f_c([\mathrm{A}],[\mathrm{B}]) \quad (1c)$$

$$\frac{\partial l_p}{\partial t} = f_p([\mathrm{A}],[\mathrm{B}]) \quad (1d)$$

where l_c and l_p are the dimensions of the crystal parallel and perpendicular to the *c*-axis, respectively, and f_c and f_p are the reaction terms parallel and perpendicular to the *c*-axis, respectively. The reaction terms, f_c and f_p, are represented as follows:

$$f_c([A],[B]) = k_1([A][B])^2 \quad (2a)$$

$$f_p([A],[B]) = k_2\{1 - \exp(-[A][B]/c_0)\} \quad (2b)$$

where k_1, k_2, and c_0 are the positive constant.

Figure 12a illustrates the results of numerical calculation regarding the crystal at $H = 0$. Near the center of the tube, the dimension along the *c*-axis grows rapidly at the earlier stage, and then stops the growth, while the dimension perpendicular to the *c*-axis grows almost constantly with time (Figure 12a). These profiles of numerical calculation closely correspond to the experimental profiles of the dumbbell crystal growth (Figure 5b). On the contrary, at the edge of the tube ($H = L/4$), the results of numerical calculation show the dimension perpendicular to the *c*-axis overcomes that along *c*-axis, which implies the formation of the thin plate crystal (Figure 12b). These results are consistent with the experimental results in the zone $H = 2.0-7.0$ cm where the crystals did not grow significantly along the *c*-axis, affording skeletal thin plates instead of dumbbells (Figure 8). Consequently, the experimental results of the morphological formation are successfully reproduced by a simple model given as a set of reaction−diffusion equations on the assumption that *the chemical reaction occurs on the crystal surface and influences the crystal growth rate*.

Conclusion

In this Article, we report an unprecedented crystal growth system of a coordination framework, where the crystallization occurs through the breaking and forming of covalent bonds. The chemical reaction simultaneous with crystal growth is the nucleophilic displacement reaction characteristic of *N*-heterocyclic chelate ligands. The reaction of hat-$(CN)_6$, ethanol, and copper(I) complex leads to the coordination framework $\{[Cu_3(CN)_3\{hat\text{-}(CN)_3(OEt)_3\}]\}_n$ (**1**), affording a variety of morphological patterns including dumbbell, cogwheel, and superlattice. The superlattice patterns are formed by the periodic ramifications at regular intervals, the periods of which range from ca. 50 to 200 μm, corresponding to ca. $(2.7-11) \times 10^4$ crystallographic unit cells. X-ray diffraction analysis indicates that there is no structural change during the growth of crystals and that these crystals are single crystals. During the formation of dumbbell crystals, growth rates parallel and perpendicular to the shaft of a dumbbell are quite different: the former shows a drastic change of growth rate, while the latter is almost constant. These results observed in the formation of dumbbell crystals are successfully reproduced by a simple model given as a set of reaction−diffusion equations, indicating that the chemical reactions on crystal surfaces play a significant role in determining the macroscopic crystal morphologies. As a consequent, if a certain chemical reaction is applied to a certain crystallization system, we can get some unprecedented morphologies reflecting the symmetry of the crystal structure. Crystallization systems involving simultaneous chemical reactions are still very rare, but we believe that this paper is a sufficient trigger for the development of this chemical-reaction-inspired crystal growth field.

(29) The characteristic time of diffusion can be estimated as l^2/D, where l is the characteristic length, and D is the diffusion constant. Here, the order of diffusion constant is assumed to be 10^{-6} cm^2 s^{-1}, and the characteristic length is 1 cm based on the length of the tube. We then can estimate the characteristic diffusion time as 10^6 s $\sim 10^2$ h. This estimation supports our discussion based on the competition between reaction and diffusion.

Acknowledgment. This work was supported by a Grant-in-Aid for Scientific Research (Priority Area, Chemistry of Coordination Space, No. 434) from The Ministry of Education, Culture, Sports, Science, and Technology of Japan.

Supporting Information Available: Crystal structure of **1**, some photographs of the skeletal thin plates of **1**, sequence photographs of the crystals of **1** growing into a dumbbell and a cogwheel, the results of simulation of X-ray diffraction patterns derived from the crystal structure of **1**, and X-ray crystallographic files (CIF). This material is available free of charge via the Internet at http://pubs.acs.org.

JA065254K